Hybrid anapole modes of high-index dielectric nanoparticles

Boris Luk'yanchuk,[1,2,3,*] Ramón Paniagua-Domínguez,[1] Arseniy I. Kuznetsov,[1]
Andrey E. Miroshnichenko,[4] and Yuri S. Kivshar[4]

[1]*Data Storage Institute, A*STAR (Agency for Science, Technology and Research), 2 Fusionopolis Way, Innovis, 138634, Singapore*
[2]*Division of Physics and Applied Physics, School of Physical and Mathematical Sciences, Nanyang Technological University, 637371 Singapore*
[3]*Faculty of Physics, Lomonosov Moscow State University, Moscow 119991, Russia*
[4]*Nonlinear Physics Centre, Research School of Physics and Engineering, Australian National University, Canberra, Australian Capital Territory 2601, Australia*

(Received 28 December 2016; published 15 June 2017)

We investigate the peculiarities of light scattering from subwavelength particles made of high-refractive-index materials caused by the coexistence of particular anapole modes of both electric and magnetic character. The similarities and differences of such anapole modes are discussed in detail. We also show that these two types of anapole modes can be supported simultaneously by subwavelength high-index spherical dielectric particles.

DOI: 10.1103/PhysRevA.95.063820

I. INTRODUCTION

Nonradiating charge-current configurations involving toroidal dipoles have attracted attention in a wide range of different fields of physics [1]. In such mode configurations, the electric and toroidal dipole modes, the so-called anapoles, cancel each other in the far field [2–4] as a consequence of both dipole modes sharing the same radiation pattern. Such anapoles were first experimentally observed in configurations involving several particles having magnetic dipole moment, such as split-ring resonators [2]. Interestingly, it has also been recently predicted that these modes may exist in the much simpler case of a single, isolated, high-index particle [3,4]. This prediction has been experimentally verified at optical frequencies with silicon nanodisks [3]. The excitation of anapole modes in small particles with high refractive index allows a dramatic reduction of their scattering cross section, which may reach values well below the Rayleigh limit for nonresonant excitation of a single electrical dipole mode [5]. So far, anapole modes have been discussed in the context of suppression of the electric dipole radiation, that is, as an interference effect due to the simultaneous excitation of the electric dipole and the electric toroidal dipole moments. The electric dipole is associated with the oscillating charges, while the toroidal dipole is associated with the poloidal current flow on the surface of a torus. However, one can imagine also the dual situation, in which magnetization currents flowing on the surface of a torus would generate a magnetic toroidal dipole mode. Under some circumstances, this magnetic toroidal moment, which would share the radiation characteristics with the conventional magnetic dipole, could also lead to the total suppression of radiation from the system (a so-called magnetic anapole).

In the present paper, we discuss the basic properties of such magnetic anapoles together with hybrid situations for which both electric and magnetic anapole modes are excited at the same frequency. We study the realization of these effects in light scattering by a spherical particle, when one can employ the exact Mie solution. Although the spherical geometry is not optimal for experimental realization of these hybrid resonances due to simultaneous excitation of higher-order multipoles, it enables understanding of the basic physics connected to these resonances.

II. MIE RESONANCES IN PARTICLES WITH HIGH REFRACTIVE INDEX

The Mie theory [6–8] represents the exact solution of Maxwell's equations for the scattering of a plane wave by a spherical particle, and it allows writing the scattering efficiency of the particle in the following simple form:

$$Q_{\mathrm{sca}} = \frac{2}{q^2}\sum_{\ell=1}^{\infty}(2\ell+1)[|a_\ell|^2+|b_\ell|^2], \tag{1}$$

where Q_{sca} represents the ratio between the scattering cross section and the geometrical cross section of the particle, $\sigma_{\mathrm{geom}} = \pi R^2$, where R is its radius. The scattering amplitudes a_ℓ (electric) and b_ℓ (magnetic) are defined by the following formulas:

$$a_\ell = \frac{F_\ell^{(a)}}{F_\ell^{(a)} + iG_\ell^{(a)}}, \quad b_\ell = \frac{F_\ell^{(b)}}{F_\ell^{(b)} + iG_\ell^{(b)}}, \tag{2}$$

and the quantities $F_\ell^{(a,b)}$ and $G_\ell^{(a,b)}$ are expressed by

$$\begin{aligned} F_\ell^{(a)} &= n\psi'_\ell(q)\psi_\ell(nq) - \psi_\ell(q)\psi'_\ell(nq), \\ G_\ell^{(a)} &= n\chi'_\ell(q)\psi_\ell(nq) - \psi'_\ell(nq)\chi_\ell(q), \\ F_\ell^{(b)} &= n\psi'_\ell(nq)\psi_\ell(q) - \psi_\ell(nq)\psi'_\ell(q), \\ G_\ell^{(b)} &= n\chi_\ell(q)\psi'_\ell(nq) - \psi_\ell(nq)\chi'_\ell(q). \end{aligned} \tag{3}$$

Here $\psi_\ell(q) = \sqrt{\frac{\pi q}{2}}J_{\ell+\frac{1}{2}}(q)$, $\chi_\ell(q) = \sqrt{\frac{\pi q}{2}}N_{\ell+\frac{1}{2}}(q)$, where $J_n(x)$ and $N_n(x)$ are the Bessel and Neumann functions; $\psi'_\ell(q) = d\psi_\ell(q)/dq$, $\chi'_\ell(q) = d\chi_\ell(q)/dq$, and $q = 2\pi R/\lambda$ is the so-called size parameter, with λ being the radiation wavelength. The particle is considered to be of an ideal spherical shape made of an isotropic, homogeneous, and nonmagnetic ($\mu = 1$) material. In addition, we consider nondissipative,

*boris_l@dsi.a-star.edu.sg

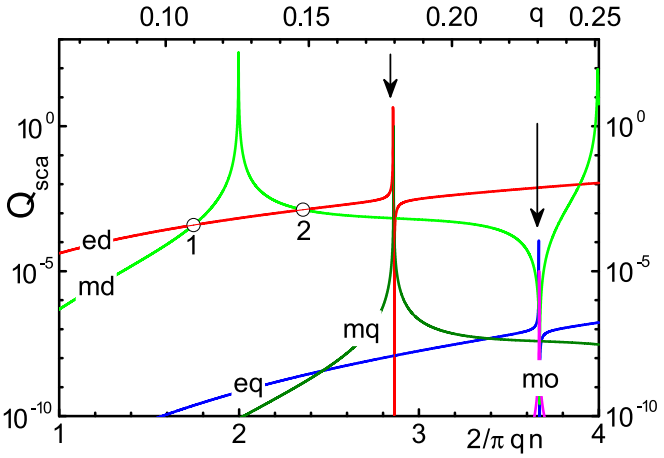

FIG. 1. Partial scattering efficiencies $Q_\ell^{(e)}$ and $Q_\ell^{(m)}$ for electric dipole (ed), quadrupole (eq), magnetic dipole (md), magnetic quadrupole (mq), and magnetic octupole (mo) modes for spherical particle with refractive index $n = 25$. The arrows indicate the positions where the electric ($q \approx 0.18$) and magnetic ($q \approx 0.23$) dipole scattering vanishes.

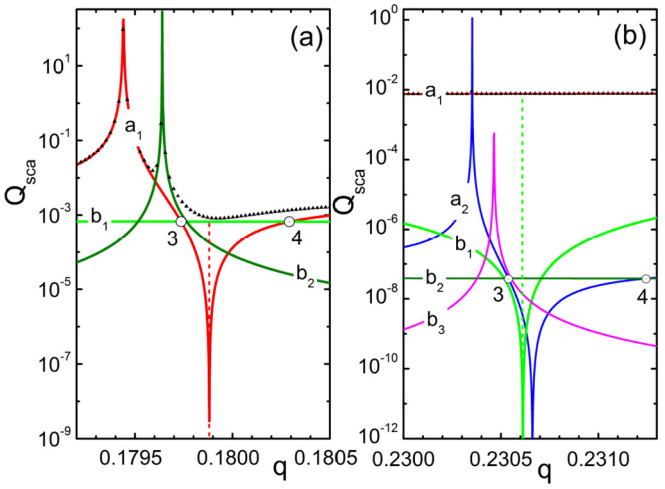

FIG. 2. Total scattering $Q_{\rm sca}$ (black triangles) and partial scattering efficiencies $Q_\ell^{(e)}$ and $Q_\ell^{(m)}$ for a particle with refractive index $n = 25$ in the range of the first electric (a) and magnetic (b) anapole modes. (a) At the point $Q_1^{(e)} = 0$ (electric anapole) the main contribution to scattering comes from the magnetic dipole $Q_1^{(m)}$. The effect of the electric quadrupole $Q_2^{(e)}$ is negligible. (b) At the point $Q_1^{(m)} = 0$ (magnetic anapole) the main contribution to the scattering comes from the electric dipole $Q_1^{(e)}$, which practically coincides with the total scattering $Q_{\rm sca}$ under Rayleigh scattering. Nearby this point, there are two closely situated resonances, corresponding to electric quadrupole $Q_2^{(e)}$ and magnetic octupole $Q_3^{(m)}$.

Im$\varepsilon = 0$, dielectric materials with high positive refractive index $n = \sqrt{\varepsilon} \gg 1$.

Inside the particle, one can find the internal field amplitudes d_ℓ (electric) and c_ℓ (magnetic) which are defined as

$$d_\ell = -\frac{in}{F_\ell^{(a)} + iG_\ell^{(a)}}, \quad c_\ell = \frac{in}{F_\ell^{(b)} + iG_\ell^{(b)}}. \tag{4}$$

The internal amplitudes d_ℓ and c_ℓ never vanish, in contrast to what may happen with the scattering amplitudes a_ℓ and b_ℓ. It is convenient to represent the total scattering efficiency in (1) as a sum of partial electric, $Q_\ell^{(e)}$, and magnetic, $Q_\ell^{(m)}$, scattering efficiencies

$$Q_{\rm sca} = \sum_{\ell=1}^{\infty} \left(Q_\ell^{(e)} + Q_\ell^{(m)}\right), \quad Q_\ell^{(e)} = \frac{2}{q^2}(2\ell+1)|a_\ell|^2,$$
$$Q_\ell^{(m)} = \frac{2}{q^2}(2\ell+1)|b_\ell|^2, \tag{5}$$

which allows identification of different contributions from the modes excited in the particle.

In Fig. 1 we show the scattering efficiencies $Q_\ell^{(e)}$ and $Q_\ell^{(m)}$ for a spherical dielectric particle with refractive index $n = 25$. In the whole range represented, the size parameter of the particle is $q < 0.25$; i.e., the particle is very small as compared to the wavelength in the ambient medium ($R < 0.04\lambda$). These partial resonances repeat periodically; e.g., magnetic dipole resonance takes place at $qn/\pi = 1,2,3\cdots$. We show in Fig. 1 a few first partial scattering efficiencies. The full picture with a larger number of scattering efficiencies is presented in Appendix A. One can see that the magnetic dipole resonance (green curve) plays the dominant role in scattering. This effect is usual in nanoparticles made of high-refractive-index dielectrics [9–13]. However, the electric dipole scattering is dominant between the resonances, due to the conditions [14] $a_\ell \propto q^{2\ell+1}$ and $b_\ell \propto q^{2\ell+3}$. Both the electric and the magnetic resonances have the typical Fano profile [5,15–17]. The only difference is that the Fano resonances associated with electrical modes are very sharp [15], while the ones associated with magnetic resonances are very broad.

Point 1 in Fig. 1 refers to the so-called Kerker's first condition, for which the particle presents near-zero back scattering. Point 2 indicates the second Kerker condition and corresponds to minimal forward scattering. This directional scattering behavior has already been discussed in a number of papers [13]. The arrows in the figure indicate the positions where electric and magnetic dipole scattering tend to zero. In Fig. 2 we show the fine structure of partial scattering efficiencies $Q_\ell^{(e)}$ and $Q_\ell^{(m)}$ in the vicinity of these zeros of electric dipole scattering $2qn/\pi \approx 2.86$ and magnetic dipole scattering $2qn/\pi \approx 3.67$.

Let us first discuss the zeros of the electric dipole scattering $Q_1^{(e)} = 0$. This condition is fulfilled along a trajectory on the plane of $\{q,n\}$ parameters. The equation describing this trajectory is given by $F_1^{(a)} = 0$, which can be recast as

$$1 - n^2 + q(n^2 - 1 + n^2q^2)\cot(q) + nq(n^2 - 1 - n^2q^2)$$
$$\times \cot(nq) + nq^2(1 - n^2)\cot(q)\cot(nq) = 0, \tag{6}$$

where we should consider only those solutions with $\cos(q) \neq 0$ and $\cos(nq) \neq 0$.

In a similar way, the zeros of magnetic dipole amplitude, $F_1^{(b)} = 0$, follow some trajectory in the $\{q,n\}$ space of parameters, in this case given by the following equation:

$$n^2 - 1 + nq[\cot(nq) - n\cot(n)] = 0. \tag{7}$$

Equations (6) and (7) are valid for arbitrary values of n and q. They have an infinite number of solutions. That

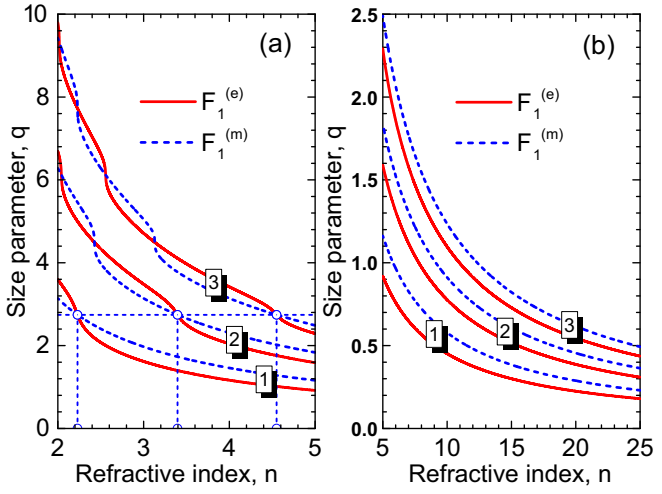

FIG. 3. Trajectories of $F_1^{(a)}(n,q) = 0$ (red) and $F_1^{(b)}(n,q) = 0$ (blue), corresponding to vanishing electric and magnetic dipole contributions, on the plane of n and q parameters for refractive index $n < 5$ (a) and $n > 5$ (b).

is, for each value of refractive index there is an infinite set of solutions with corresponding size parameter q. The first three roots of the solutions of Eqs. (6) and (7) are shown in Fig. 3. For moderate values of the refractive index ($n < 5$) one can see an intertwining braid structure for the corresponding trajectories in Fig. 3(a), crossing each other several times. However, for larger values of the refractive index ($n > 5$) these braids untwine [see Fig. 3(b)] and the trajectories stop crossing each other. From Fig. 3(a) it can be seen that there is a discrete set of values of the size parameter ($q = 2.7437,\ 4.4934,\ 6.1168\cdots$) for which Eqs. (6) and (7) are fulfilled simultaneously, that is, for which electric and magnetic dipoles are simultaneously zero. Moreover, for each q value there is a discrete set of appropriate n values [for example, $q = 2.7437$ yields $n = 2.2294$, 3.3956, and 4.5508, as seen in Fig. 3(a)]. One can see a similar discrete set of n values at $q = 4.4934$ and higher values.

III. ELECTRIC AND MAGNETIC ANAPOLE MODES

In order to have a deeper insight into the origin of excited anapole modes, in Fig. 4 we show the distribution of electric and magnetic fields and the Poynting vector around and inside a spherical particle at the electric anapole frequency corresponding to $n = 25$ and $q = 0.179\,88$. The upper row in Figs. 4 [panels (a–c)] shows two-dimensional (2D) maps of the field distribution inside the particle and in the near-field area outside the particle, while the lower row [panels (d–f)] shows the three-dimensional (3D) field distribution inside the particle. In particular, Fig. 4(a) represents the electric

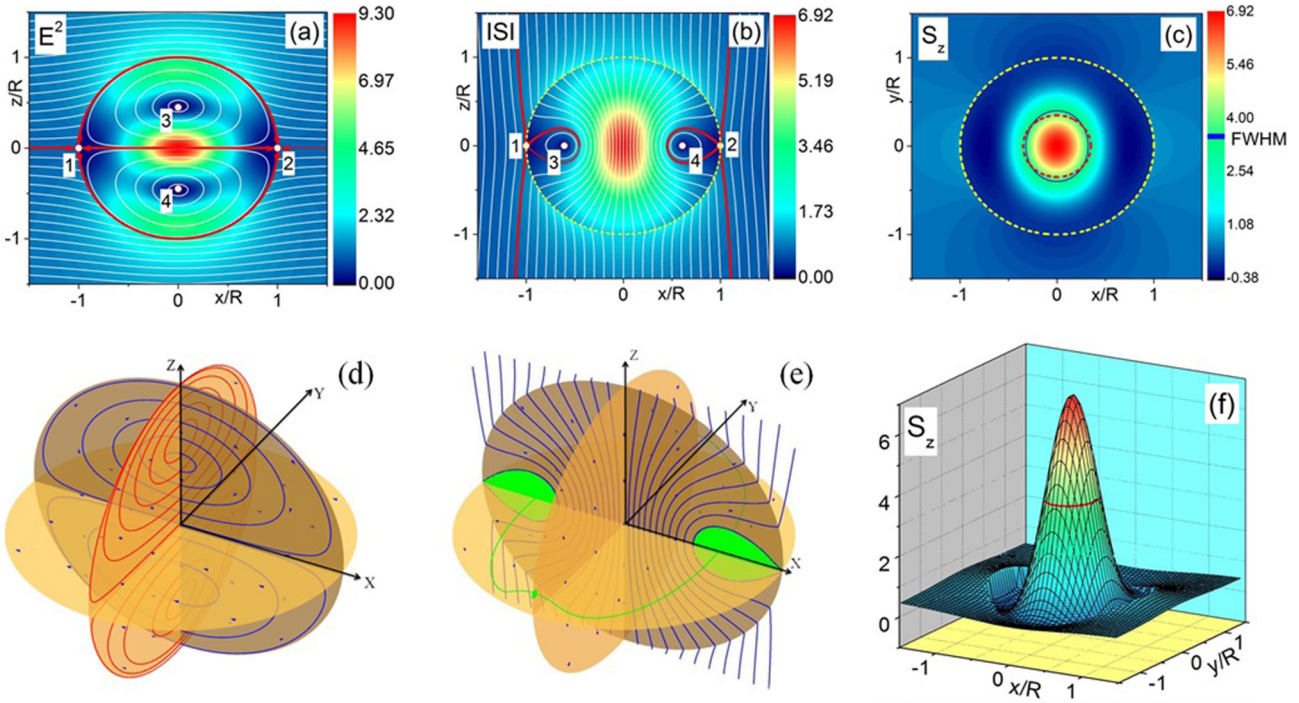

FIG. 4. Distribution of electric and magnetic fields and Poynting vector for a spherical particle with $q = 0.179\,88$ and $n = 25$. The upper row (a–c) shows the 2D distributions and the lower row (d–f) shows the 3D distributions. (a) Map of the distribution of electric field intensity $\mathbf{E}^2$ in the $\{x,z\}$ plane. The white lines represent the electric field lines. (b) Map of the modulus of Poynting vector $|\mathbf{S}|$ in the $\{x,z\}$ plane. The white lines represent the vector field lines. (c) Distribution of the z component of the Poynting vector in the $\{x,y\}$ plane through the particle diameter. The red dashed line indicates diffraction limit size, $\pi/2qn \approx 0.35$, and the blue line indicates the full width at half maximum (FWHM). (d) Electric field lines in the $\{x,z\}$ plane (blue) and magnetic field lines in the perpendicular $\{y,z\}$ plane (red). (e) Singular line (green) with zero Poynting vector $\mathbf{S}(x,y,z) = 0$ passing through the particle. This line enters into unstable focal points at the $\{x,z\}$ plane. Unstable phase trajectories starting at these focal points fill the whole region indicated by green areas. It refers to zero field regions. (f) Intensity distribution in the $\{x,y\}$ plane through the particle diameter. The level $|\mathbf{S}| \approx 3.5$ (red line) corresponds to FWHM.

field intensity distribution ($\mathbf{E}^2$) within the $\{x,z\}$ plane, with the corresponding white lines represent the lines of electric field vector $\mathbf{E}$. One can easily identify the poloidal current distribution of the electric vector inside the nanoparticle. The red lines in the figure represent the calculated separatrices. There are four singular points in the field distribution, points 1 and 2 corresponding to saddles, and points 3 and 4 corresponding to field zeros. In the 3D picture in Fig. 4(d) we show the electric field lines within the $\{x,z\}$ plane (blue lines) and the magnetic field lines within the perpendicular $\{y,z\}$ plane (red lines).

In Fig. 4(b) we show the distribution of the Poynting vector within the $\{x,z\}$ plane. Note that there is almost no energy flow in the region inside the loops of separatrices around the focal points 3 and 4. It is interesting to view the electric anapole as an equivalent to a confocal system of two lenses with numerical aperture (NA) close to unity. Although the full number of modes [18] is taken into account, the calculations show a minimal distortion of the Poynting vector outside the particle. In the 3D plot in Fig. 4(e), the Poynting vector in the $\{x,z\}$ plane is shown by blue lines. The green, 3D line presents a singularity characterized by a zero Poynting vector. The green areas—large in the $\{x,z\}$ plane and small in the perpendicular $\{y,z\}$ plane—show the region with almost no energy flow [one can see in Fig. 4(c) that the field compression is stronger along the x axes].

A. Toroidal dipole moments in a Cartesian basis

The contribution of electric toroidal dipole moment to the electric anapole can be clearly seen if one performs a multipolar decomposition using a Cartesian basis (see Appendix B), similar to what has been shown previously in Fig. 2(c) of Ref. [3] for $n = 4$. The scattering at the electric anapole mode ($n = 25$ and $q = 0.179\,88$) reaches a value as low as $Q_{\text{sca}} \approx 8.5 \times 10^{-4}$ [see Fig. 2(a)] suppressed even compared to the Rayleigh limit given by $Q_{\text{sca}}^{(Ra)} = \frac{8}{3}(\frac{\varepsilon-1}{\varepsilon+2})^2 q^4 \approx 2.8 \times 10^{-3}$.

By performing a similar analysis at the magnetic anapole frequency (shown in Fig. 9) it can be seen that the zero in the b_1 coefficient arises as a result of the destructive interference of the radiation from the Cartesian magnetic dipole, with the usual definition in terms of the particle internal fields, $\mathbf{m} = \frac{-i\pi c}{\lambda}\int \varepsilon_0(n^2-1)[\mathbf{r}\times\mathbf{E}]d\mathbf{r}$ (note that this expression holds for a particle in vacuum) and the so-called mean radii distribution of the magnetic dipole, defined [19] as $\bar{R}_m^2 = \frac{-i\pi c}{10\lambda}\int \varepsilon_0(n^2-1)[\mathbf{r}\times\mathbf{E}]r^2 d\mathbf{r}$. This contribution can be obtained as a third-order term in the expansion of the exact magnetic dipole moment [20] and share the same radiation pattern as the Cartesian magnetic dipole, thus being able to interfere with it. To get proper insight into the physics of the magnetic anapole, in Fig. 5 we show the field distributions for a particle with $q = 0.230\,62$ and $n = 25$. The upper row [panels (a–c)] shows the 2D field distributions inside the particle and in the near-field area outside the particle, while the lower

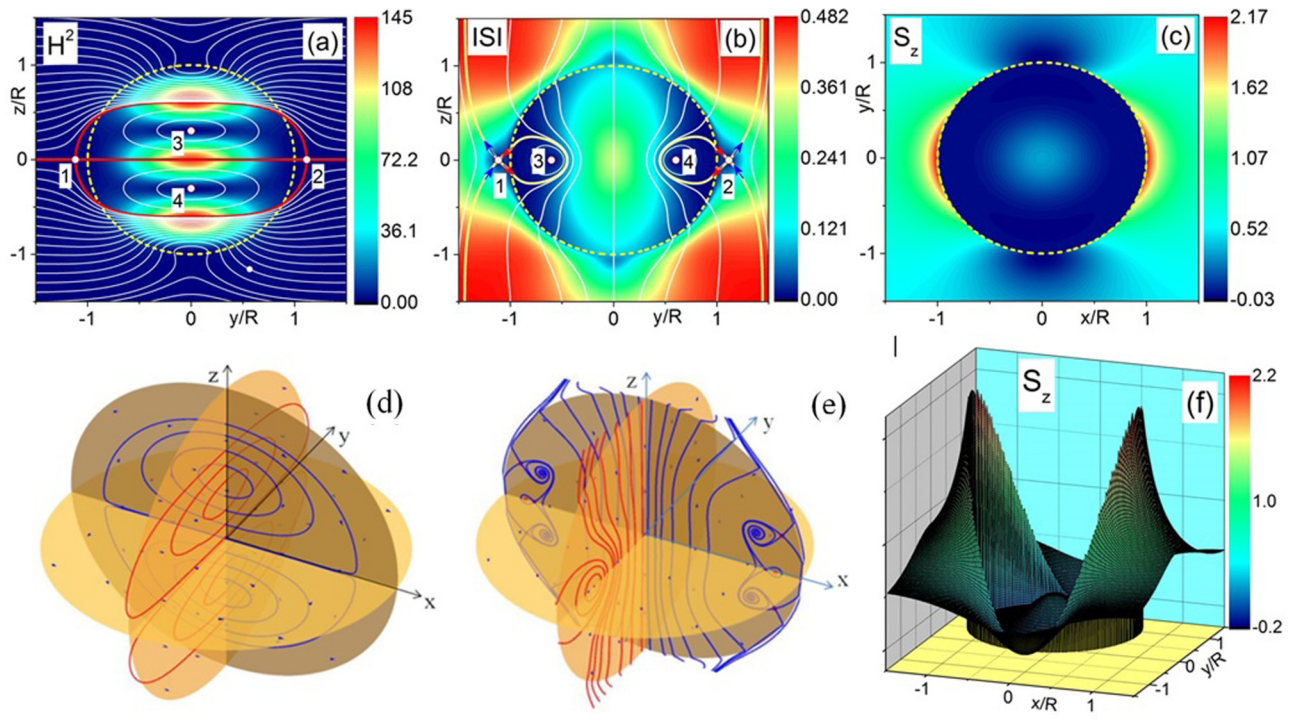

FIG. 5. Distribution of magnetic and electric fields and Poynting vector for a spherical particle with $q = 0.230\,62$ and $n = 25$. The upper row (a–c) shows the 2D distributions and the lower row (d–f) shows the 3D distributions. (a) Distribution of magnetic field intensity ($\mathbf{H}^2$) in the $\{y,z\}$ plane passing through the particle diameter. The white lines represent the magnetic field lines. (b) Map of the modulus of the Poynting vector $|\mathbf{S}|$ in the $\{y,z\}$ plane. The white lines represent the vector field lines. (c) Distribution of the S_z component of the Poynting vector in the $\{x,y\}$ plane passing through the particle diameter. (d) 3D representation of the electric field lines (blue) in the $\{x,z\}$ plane and magnetic field lines (red) in the perpendicular $\{y,z\}$ plane. (e) Poynting vector lines through the particle cross sections in the $\{x,z\}$ plane (blue) and the $\{y,z\}$ plane (red). (f) Distribution of the z component of the Poynting vector in the $\{x,y\}$ plane passing through the particle diameter.

row [panels (d–f)] shows the 3D field distributions inside the particle. In this case, Fig. 5(a) represents the distribution of magnetic field intensity $\mathbf{H}^2$ in the $\{y,z\}$ plane and the white lines represent the lines of magnetic field vector $\mathbf{H}$. From this plot, it is possible to identify the poloidal distribution of the magnetic vector field inside the nanoparticle. The red lines again represent the separatrices. Analogously to the electric anapole, there are four singular points, points 1 and 2 corresponding to saddles, and points 3 and 4 corresponding to field zeros. In the 3D picture of Fig. 5(d) we show the electric field lines within the $\{x,z\}$ plane as blue lines and the magnetic field lines within the perpendicular $\{y,z\}$ plane as red lines. In general, this picture is quite similar to that of Fig. 4(d). The saddle points 1 and 2 in Fig. 5(a) are outside the particle. As a result the magnetic toroidal field also can be outside the particle while the electrical toroidal field is confined inside the particle.

In Fig. 5(b) we show distribution of the Poynting vector in the $\{y,z\}$ plane. The distribution of the Poynting vector in the plane of magnetic polarization $\{y,z\}$ at the magnetic anapole frequency looks qualitatively similar to the distribution of the Poynting vector in the plane of electric polarization $\{x,z\}$ at the electric anapole [see Fig. 4(b)]. Both distributions have two saddle points (indicated by 1 and 2 in the figure) and two loops of separatrices around the focal points (indicated by 3 and 4 in the figure). As in the case of the electrical anapole, there is almost no energy flow within the region inside the loops of the separatrices around the focal points 3 and 4. However, in contrast to the electric anapole, in which the energy is "pulled" inside the particle, in the case of the magnetic anapole the energy is "pushed" outside the particle, and creates near-field enhancement similar to the plasmonic particle. It can be clearly seen in Figs. 5(c) and 5(f), which show the energy distribution (z component of the Poynting vector) within the $\{x,y\}$ plane passing through the particle diameter. The diffraction limit diameter with $\pi/2qn \approx 0.27$ is presented in Fig. 5(c) by the cyan dashed line.

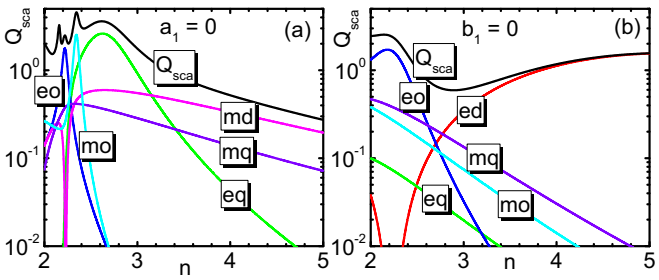

FIG. 6. (a) Total scattering efficiency and partial scattering amplitudes $Q_\ell^{(e)}$ and $Q_\ell^{(m)}$ as a function of the refractive index n along the trajectory of zero electric dipole (electric anapole mode) in the parameter space $\{q,n\}$; i.e., the size parameter, $q = q(n)$, follows the first root of the equation $F_1^{(a)}(n,q) = 0$ [see Fig. 3(a)]. (b) Total scattering efficiency and partial scattering amplitudes $Q_\ell^{(e)}$ and $Q_\ell^{(m)}$ as a function of the refractive index n along the trajectory of the magnetic anapole mode; i.e., the size parameter, $q = q(n)$, follows the first root of the equation $F_1^{(b)}(n,q) = 0$ [see Fig. 3(a)].

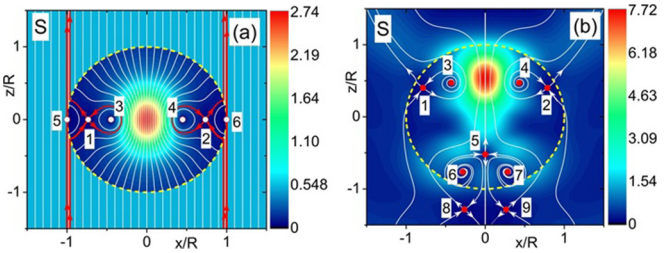

FIG. 7. (a) Poynting vector distribution calculated for a spherical particle with $q = 2.7437$ and $n = 2.2294$ under the dipole approximation, $\ell = 1$. The color map represents the modulus of the Poynting vector $|\mathbf{S}|$ and the white lines the vector field lines. The separatrices are shown by red lines and the singular points are indicated by numbers. (b) The same as in (a) but the full number of modes [18] $\ell_{\max} = |q + 4.05q^{1/3} + 2|$ is taken into account. There are seven singular points inside the particle in this case, including three saddles and four focal points. Two additional saddle points can be seen near the surface, outside the particle.

IV. EFFECT OF HIGHER-ORDER MODES

Note that, thanks to the large refractive index chosen, it is possible to visualize the field distributions corresponding to the anapole modes without much distortion coming from the higher-order multipolar contributions. In fact, for refractive indices $n > 5$ and for the first root of vanishing dipole contributions the corresponding size parameters are less than unity. Thus in this range of values of the refractive index

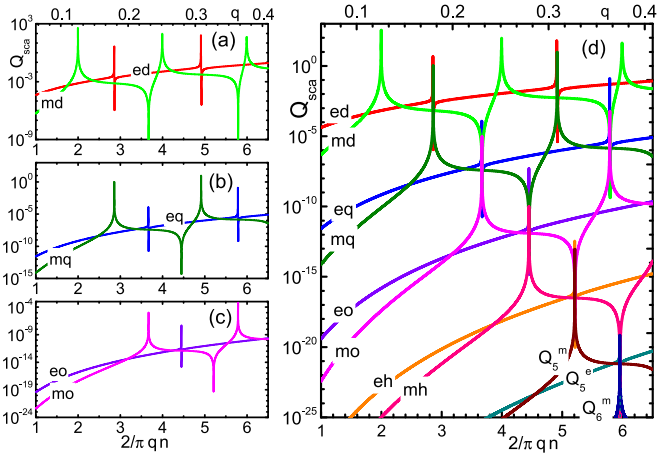

FIG. 8. Partial scattering efficiencies for spherical particle with refractive index $n = 25$. Electric efficiencies $Q_\ell^{(e)}$ are shown for electric dipole (ed), quadrupole (eq), octupole (eo), hexadecapole (eh), and higher-order modes. Magnetic scattering efficiencies $Q_\ell^{(m)}$ marked by "m"—magnetic dipole (md), magnetic quadrupole (mq), etc. Left panels show, correspondingly, pairs of electric and magnetic scattering efficiencies for dipole (a), quadrupole (b), and octupole (o) modes. Variation of the electric Fano resonances is very sharp and appears to be like vertical lines. More precisely the structure of the electric Fano resonance is shown in Fig. 9(a). The right panel (d) presents all modes together. It shows characteristic clusters of modes for high refractive index, e.g., electric dipole almost coincides with magnetic quadrupole, electric quadrupole with magnetic octupole, etc.

only the electric and magnetic dipole scattering amplitudes $Q_1^{(e)}$ and $Q_1^{(m)}$ contribute significantly in the vicinity of magnetic and electric anapoles, respectively. However, for $n < 5$ the scattering amplitudes of the higher-order modes yield important contributions to the total efficiency, as shown in Fig. 6. Figure 6(a) shows the total scattering and partial scattering contributions as a function of the index of refraction along the trajectory of zero electric dipole, $a_1 = 0$ (electric anapole) in the parameter space $\{q,n\}$. From this plot it is seen that the magnetic dipole yields the dominant contribution, e.g., for $n > 3.5$. A similar behavior is found when analyzing the contributions along the trajectory of zero magnetic dipole, $b_1 = 0$ (magnetic anapole), shown in Fig. 6(b).

From the results presented in Fig. 6 it is clear that, due to the contribution of the higher-order modes, field distributions at the anapole modes for $n < 3.5$ will mainly be determined by the higher-order modes. A particularly interesting example is the one given by $n = 2.2294$ and $q = 2.7437$, when both amplitudes a_1 and b_1 tend to zero simultaneously [see Fig. 3(a)]. In this situation, the field distribution of the "ideal double anapole" [obtained within the dipole approximation; see Fig. 7(a)] is strongly distorted by the contributions of higher-order modes, as shown in Fig. 7(b). In particular, the nonradiating currents forming a loop around the singular points 3 and 4 in Fig. 7(a) (and whose number increases with the order of the anapole; see Appendix C) transform into radiating currents around the singular points 3 and 4 in Fig. 7(b). While the spherical geometry allows suppressing the electric and magnetic dipole moments, it does not allow doing the same with the quadrupole and octupole modes simultaneously, as seen in Fig. 6. Nevertheless, by using nonspherical geometries, e.g., disks or spheroids, or layered structures, it could be possible in principle to simultaneously suppress higher-order multipolar contributions.

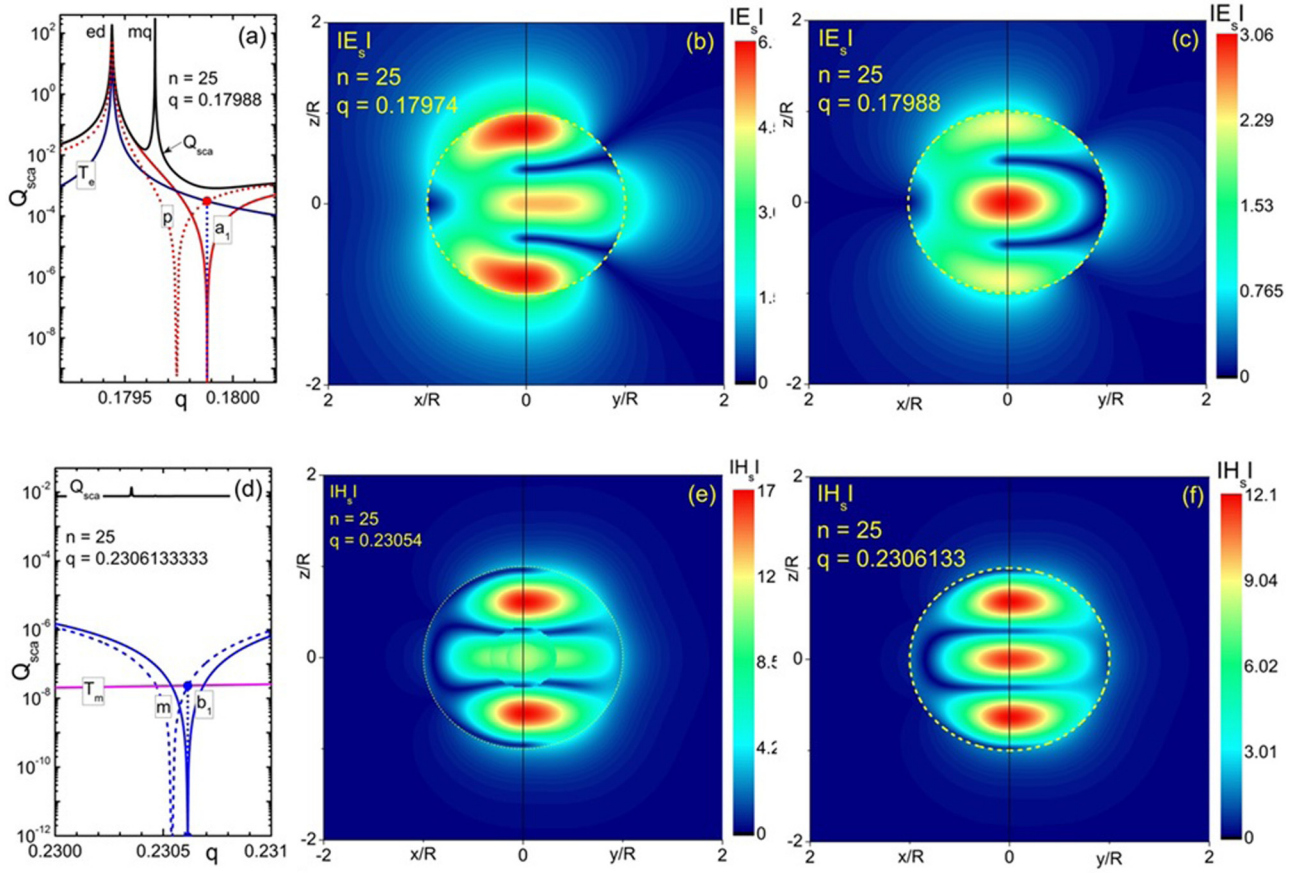

FIG. 9. Cartesian multipole analysis of the $n = 25$ sphere and the correspondence with the spherical (Mie) multipoles. Panels (a–c) represent the electric anapole mode ($a_1 = 0$) and panels (d–f) represent the magnetic anapole mode ($b_1 = 0$). Panel (a) shows the scattering efficiency Q_{sca} and partial electric dipole scattering efficiency from the Mie theory (indicated as a_1). The other two curves represent the amplitudes of the Cartesian electric dipole **p** and the electric toroidal dipole $\mathbf{T}_e$. A similar analysis, and the corresponding expressions for these terms, can be found in Ref. [3]. These two amplitudes have the opposite phases and their sum coincides with the scattering of the spherical electric dipole a_1. These modes **p** and $\mathbf{T}_e$ exactly compensate each other at the point $a_1 = 0$. Panels (b,c) show the electric field maps in the $\{x,z\}$ and the $\{y,z\}$ planes at the position of vanishing Cartesian (b) and Mie theory (c) electrical dipoles. Here we present the internal fields and scattered fields only. Panel (d) shows the scattering efficiency Q_{sca} and partial magnetic dipole scattering efficiency from the Mie theory (indicated as b_1). The other two curves represent the amplitudes of Cartesian magnetic dipole **m** and what we refer to as the toroidal magnetic dipole $\mathbf{T}_m$, which has been previously named the mean radii correction [19]. Once again these two amplitudes have opposite phases and their sum coincides with the scattering of the spherical magnetic dipole b_1. These two modes **m** and $\mathbf{T}_m$ exactly compensate each other at the point $b_1 = 0$. Panels (e,f) show the magnetic field maps in the $\{x,z\}$ and the $\{y,z\}$ planes at the position of vanishing Cartesian (e) and Mie theory (f) magnetic dipoles. Here we present the internal fields and scattered fields only.

V. OUTLOOK

To conclude, we have shown that two types of anapole modes, namely, electric and magnetic, can be observed in the light scattering from a single spherical particle with high refractive index, with important differences between them. First, the excitation of the magnetic toroidal mode can only be realized for larger size parameters, which typically yields higher contributions from the rest of the modes excited. Second, these two types of anapoles have significant differences in the energy flow. While the electric anapole concentrates the energy inside the particle, the magnetic anapole concentrates the energy outside the particle, in some way similar to plasmonic particles. This is a generic effect which is repeatedly found for all subsequent zeros of the dipolar scattering in a sphere with fixed refractive index. For example, for a sphere with $n = 25$, the second zeros of dipole scattering (for increasing size parameter) is found for the electric dipole at $q = 0.309\,26$, and the magnetic dipole at $q = 0.353\,92$ [see Fig. 3(b)], which shows qualitatively the same behavior as that of Figs. 4(c), 4(f), 5(c), and 5(f).

Finally, we have also shown that both types of anapole modes can be excited simultaneously, resulting in the formation of hybrid anapole modes. However, for spherical particles this effect is hindered by the partial contributions from higher-order modes, which lead to the formation of nontrivial field configurations with vortices and singularities inside and outside the particle. We foresee, nevertheless, that this limitation could be overcome exploring other geometrical shapes (such as disks or spheroids) or multilayered configurations. Using the same approach, the anapole concept (nontrivial, nonradiating current distributions) can further be generalized to any higher order in Mie theory (e.g., a zero in the a_2 coefficient, the electric quadrupolar anapole, is achieved when the Cartesian electric quadrupole compensates the toroidal quadrupole and the mean radii of the toroidal distribution).

ACKNOWLEDGMENTS

The authors B.L., R.P.D., and A.K. acknowledge support by the Data Storage Institute core funds and the A*STAR SERC Pharos program, Grant No. 152 73 00025 (Singapore). B.L. also acknowledges support by the Russian Ministry of Education and Science (Grant No. 14.W03.31.0008). A.M. and Y.K. are thankful to the Australian Research Council.

APPENDIX A: PARTIAL SCATTERING EFFICIENCIES

The partial scattering efficiencies corresponding to the electric dipole (ed), quadrupole (eq), octupole (eo), hexadecapole (eh) and higher order contributions are plotted in a broad range of $\{q,n\}$ parameteres in Fig. 8.

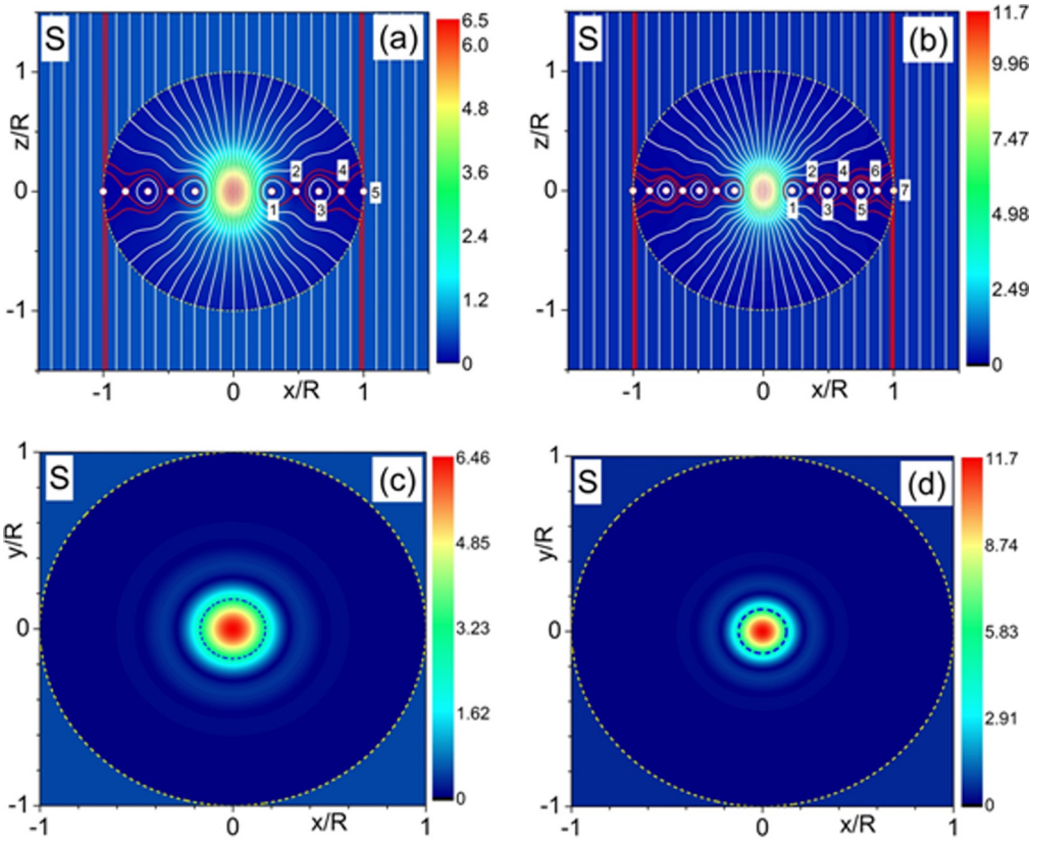

FIG. 10. Poynting vector distribution in the $\{x,z\}$ plane calculated under dipole approximation, $\ell = 1$, with $q = 2.7437$, $n = 3.3956$ (a), and $n = 4.5508$ (b). Color panel presents the modulus of the Poynting vector $|\mathbf{S}|$. Coordinates x and z are normalized to the particle radius. (c,d) show distribution of the Poynting vector in the $\{x,y\}$ plane. Blue dashed lines indicate diffraction limit sizes.

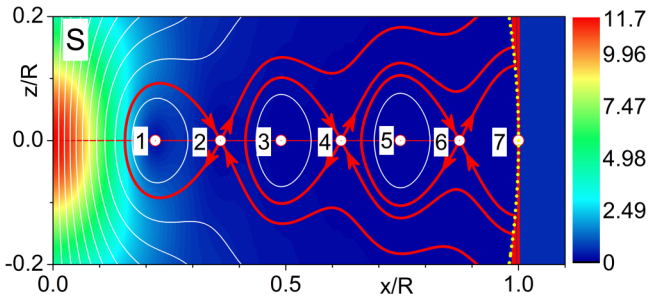

FIG. 11. Fragment of the Poynting vector distribution for $n = 4.5508$, $q = 2.7437$ under dipole approximation, $\ell = 1$.

APPENDIX B: DECOMPOSITION OF THE SCATTERING IN SPHERICAL AND CARTESIAN MULTIPOLES

An analysis of the scattering contributions for the sphere with refractive index $n = 25$ based on a Cartesian multipolar decomposition can be found in Fig. 9, together with the corresponding spherical (Mie) multipoles.

APPENDIX C: MULTIPLE TOROIDAL VORTICES FOR HIGHER-ORDER DIPOLE MODES

The hybrid anapole modes are solutions of the equations yielding $a_1 = 0$ and $b_1 = 0$. These equations have several roots. In Fig. 10, we present two roots along the size parameter $q = 2.7437$, namely, those corresponding to the refractive indices $n = 3.3956$ and $n = 4.5508$. We show the distribution of the Poynting vector at these hybrid anapole modes. Red lines show the separatrices. Note that the number of separatrix loops increases for larger refractive index values. Figures 10(a) and 10(b) show the distribution of the Poynting vector in the $\{x,z\}$ plane and Figs. 10(c) and 10(d) in the $\{x,y\}$ plane.

We show in Fig. 11 the closeup for the energy flow within the region of separatrix loops at $n = 4.5507$. With $n \gg 1$ it is possible to reach extrahigh intensity in the center of the sphere. High refractive index permits keeping the dominant role of dipole resonances for small size parameter together with conditions necessary for resonant behavior of scattering; i.e., $\pi/n < q \ll 1$. Although it is highly complicated to fulfill such conditions at the visible range of the spectrum it is possible to reach in the microwave regime, where the dielectric permittivity of some weakly dissipating ceramics reaches values of $\varepsilon \approx 1000$ [21].

[1] N. Papasimakis, V. A. Fedotov, V. Savinov, T. A. Raybould, and N. I. Zheludev, Electromagnetic toroidal excitations in matter and free space, Nat. Mater. **15**, 263 (2016).

[2] V. A. Fedotov, A. V. Rogacheva, V. Savinov, D. P. Tsai, and N. I. Zheludev, Resonant transparency and non-trivial non-radiating excitations in toroidal metamaterials, Sci. Rep. **3**, 2967 (2013).

[3] A. E. Miroshnichenko, A. B. Evlyukhin, Y. F. Yu, R. M Bakker, A. Chipouline, A.I. Kuznetsov, B. Luk'yanchuk, B. N. Chichkov, and Y. S. Kivshar, Nonradiating anapole modes in dielectric nanoparticles, Nat. Commun. **6**, 8069 (2015).

[4] W. Liu, J. Zhang, B. Lei, H. Hu, and A. E. Miroshnichenko, Invisible nanowires with interfering electric and toroidal dipoles, Opt. Lett. **40**, 2293 (2015).

[5] B. Luk'yanchuk, R. Paniagua-Domínguez, A. I. Kuznetsov, A. E. Miroshnichenko, and Y. S. Kivshar, Suppression of scattering for small dielectric particles: Anapole mode and invisibility, Phil. Trans. R. Soc. A **375**, 20160069 (2017).

[6] H. C. van de Hulst, *Light Scattering by Small Particles* (Dover, New York, 2005).

[7] M. Born and E. Wolf, *Principles of Optics*, 7th ed. (Cambridge University Press, Cambridge, 1999).

[8] C. F. Bohren and D. R. Huffman, *Absorption and Scattering of Light by Small Particles* (Wiley, New York, 1998).

[9] A. B. Evlyukhin, C. Reinhardt, A. Seidel, B. Luk'yanchuk, and B. N. Chichkov, Optical response features of Si-nanoparticle arrays, Phys. Rev. B **82**, 045404, (2010).

[10] A. Garcia-Etxarri, R. Gomez-Medina, L. S. Froufe-Perez, C. Lopez, L. Chantada, F. Scheffold, J. Aizpurua, M. Nieto-Vesperinas, and J. J. Sáenz, Strong magnetic response of submicron silicon particles in the infrared, Opt. Express **19**, 4815, (2011).

[11] A. I. Kuznetsov, A. E. Miroshnichenko, Y. H. Fu, J. B. Zhang, and B. Luk'yanchuk, Magnetic light, Sci. Rep. **2**, 492, (2012).

[12] A. B. Evlyukhin, S. M. Novikov, U. Zywietz, R. L. Eriksen, C. Reinhardt, S. I. Bozhevolnyi, and B. N. Chichkov, Demonstration of magnetic dipole resonances of dielectric nanospheres in the visible region, Nano Lett. **12**, 3749 (2012).

[13] A. I. Kuznetsov, A. E. Miroshnichenko, M. L. Brongersma, Y. S. Kivshar, and B. Luk'yanchuk, Optically resonant dielectric nanostructures, Science **354**, aag2472 (2016).

[14] Z. B. Wang, B. S. Luk'yanchuk, M. H. Hong, Y. Lin, and T. C. Chong, Energy flow around a small particle investigated by classical Mie theory, Phys. Rev. B **70**, 035418 (2004).

[15] M. I. Tribelsky and A. E. Miroshnichenko, Giant in-particle field concentration and Fano resonances at light scattering by high-refractive index particles, Phys. Rev. A **93**, 053837 (2016).

[16] A. E. Miroshnichenko, S. Flach, and Y. S. Kivshar, Fano resonances in nanoscale structures, Rev. Mod. Phys. **82**, 2257 (2010).

[17] B. Luk'yanchuk, N. I. Zheludev, S. A. Maier, N. J. Halas, P. Nordlander, H. Giessen, and C. T. ChongThe Fano resonance in plasmonic nanostructures and metamaterials, Nat. Mater. **9**, 707 (2010).

[18] P. W. Barber and S. C. Hill, *Light Scattering by Particles: Computational Methods* (World Scientific, Singapore, 1990).

[19] E. E. Radescu and G. Vaman, Exact calculation of the angular momentum loss, recoil force, and radiation intensity for an arbitrary source in terms of electric, magnetic, and toroid multipoles, Phys. Rev. E **65**, 046609 (2002).

[20] R. Fernández-Corbatón, S. Nanz, R. Alaee, and C. Rockstuhl, Exact dipolar moments of a localized electric current distribution, Opt. Express **23**, 33044 (2015).

[21] M. Song, P. Belov, and P. Kapitanova, Wireless power transfer based on dielectric resonators with colossal permittivity, Appl. Phys. Lett. **109**, 223902 (2016).